SAND2022-6654J

Validation of calibrated k-ϵ model parameters for jet-in-crossflow

Nathan E. Miller*, Steven J. Beresh†
Sandia National Laboratories, Albuquerque, NM 87185

Jaideep Ray‡
Sandia National Laboratories§, Livermore, CA 94550

Previous efforts determined a set of calibrated, optimal model parameter values for Reynolds-Averaged Navier Stokes (RANS) simulations of a compressible jet in crossflow (JIC) using a k-ϵ turbulence model. These parameters were derived by comparing simulation results to Particle Image Velocimetry (PIV) data of a complementary JIC experiment under a limited set of flow conditions. Here, a k-ϵ model using both nominal and calibrated parameters is validated against PIV data acquired from a much wider variety of JIC cases, including a realistic flight vehicle. The results from the simulations using the calibrated model parameters showed considerable improvements over those using the nominal values, even for cases that were not used in the calibration procedure that defined the optimal parameters. This improvement is demonstrated using a number of quality metrics that test the spatial alignment of the jet core, the magnitudes of multiple flow variables, and the location and strengths of vortices in the counter-rotating vortex cores on the PIV planes. These results suggest that the calibrated parameters have applicability well outside the specific flow case used in defining them and that with the right model parameters, RANS solutions for the JIC can be improved significantly over those obtained from the nominal model.

Nomenclature

C_{nom}	Nominal RANS model parameters
C_{opt}	Optimal RANS model parameters
$corr$	Two-dimensional correlation coefficient
E^*	Normalized Euclidian distance between vortex core centers
J	Jet-to-freestream dynamic pressure ratio
GME	Normalized geometric mean of the error
k	Turbulence kinetic energy
MSE	Normalized mean squared error
P	Perimeter of a vortex core
P^*	Normalized vortex perimeter
$\overline{V_x}, \overline{V_y}, \overline{V_z}$	Reynolds-averaged velocity components
X_P	A dependent variable from the PIV
X_R	A dependent variable from RANS
α	Nozzle's lateral cant angle with respect to the wall normal
Γ	Integrated circulation within a vortex core
Γ^*	Normalized vortex core circulation

Presented as Paper 2019-3706 at the AIAA AVIATION 2019 Forum, Dallas, TX, June 17–21, 2019

*Senior Member of the Technical Staff, Aerosciences Department, nmille1@sandia.gov

†Distinguished Member of the Technical Staff, Aerosciences Department, sjberes@sandia.gov

‡Distinguished Member of the Technical Staff, Extreme-scale Data Science & Analytics, jairay@sandia.gov

§Sandia National Laboratories is a multimission laboratory managed and operated by National Technology & Engineering Solutions of Sandia, LLC, a wholly owned subsidiary of Honeywell International Inc., for the U.S. Department of Energy's National Nuclear Security Administration under contract DE-NA0003525. This paper describes objective technical results and analysis. Any subjective views or opinions that might be expressed in the paper do not necessarily represent the views of the U.S. Department of Energy or the United States Government.

ϵ	Turbulent energy dissipation rate
$\overline{\omega}$	Mean streamwise vorticity

Sub/superscript

P	Data from the PIV
R	Data from RANS
$-, +$	Related to the negatively and positively oriented vortex cores, respectively

I. Introduction

The jet-in-crossflow (JIC) problem has been investigated via a large number of both experimental and numerical studies (e.g., [1, 2]), with interest related to a variety of applications including film cooling, flight vehicle attitude and roll control, and fuel injection (e.g., [3, 4]). These studies have provided considerable understanding of the flow topology and statistics [5, 6]. The flowfield is typified by a counter-rotating vortex pair (CVP) oriented in the streamwise direction in the jet core and a horseshoe vortex (HSV) near the wall which wraps around the jet column [7, 8]. For applications related to flight vehicles, the interaction of the CVP and HSV with downstream control surfaces, like fins, has been shown to modulate the forces generated by those surfaces by altering their effective angle of attack [9–11].

For the purposes of vehicle design, accurate modeling of the complex flow features at downstream control surfaces is a primary goal [12]. Unfortunately, most high-fidelity numerical approaches are so computationally expensive that Reynolds-Averaged Navier Stokes (RANS) continues to be the most efficient investigative technique. Arunajatesan [13] tested multiple two-equation RANS models for simulating a supersonic jet in a transonic, compressible crossflow and concluded that most of their predictive capabilities were “marginal at best." Although the RANS results were qualitatively similar to the experimental data used for comparison, inaccuracies in the turbulent stress predictions resulted in the incorrect location and strength of the CVP and an overpredicted velocity deficit in the jet core. These shortcomings will, in turn, lead to poor estimations of the effective forces on downstream control surfaces [14, 15].

RANS models contain many approximations which make them inaccurate. One conceptually simple way of improving their accuracy is to calibrate them (estimate the parameters in RANS models) to experimental data collected from flow configurations similar to the final use-case of the model. Duraisamy et al. [16], Xiao and Cinnella [17], and Zhang et al. [18] have all offered reviews of data-driven modeling to improve the predictive skill of RANS. Of late, these calibration activities have employed Bayesian inference, as the method allows one to capture the uncertainty/errors in the estimated parameters by treating them as random variables and computing their joint probability density function (PDF). The first attempts targeted “1D” flows e.g., turbulent channel and flat-plate boundary layers [19, 20]. Later, authors estimated the parameters of a k-ϵ model for incompressible flows, with one example being flow in urban canyons from wind-tunnel data [21]. The parameters of a k-ω-γ turbulence model for hypersonic transitional flows have also been investigated, via Bayesian calibration and Stanton number measurements from a flow over a flat plate [22]. While most of these studies used Markov chain Monte Carlo to construct the joint PDF, some studies have explored the use of ensemble Kalman filters for calibration purposes using data from simple flow configurations e.g., backward-facing step [23] as well as more complex ones such as flows over an airfoil and a wing [24].

The RANS data used by Arunajatesan [13] were produced using nominal model parameters (C_{nom}), those typically used for a variety of flow applications, without any additional calibrating to the JIC problem specifically. This led Ray et al. [25] to investigate the usefulness of rigorously tuning the parameters of the k-ϵ model in hopes of producing the best possible results. Without making structural changes to the turbulent stress model within a RANS approach, the best results that can be accomplished come by calibrating the model’s existing parameters to the exact flow case of interest. The methodology for estimating the k-ϵ parameters used in this study are described in Ray et al. [25–27], which also explored (and then rejected) the possibility of using quadratic and cubic eddy-viscosity models in the context of JIC configurations. Ray et al. [25] proposed a Bayesian inverse problem and a Markov chain Monte Carlo method utilizing particle image velocimetry (PIV) data of the mean streamwise vorticity ($\overline{\omega}$) to determine an optimum, calibrated combination of the three model parameters (C_{opt}) for a single case of the jet-in-crossflow problem. Ray et al. [27] continued this work by calibrating the parameters for a wider set of flow cases and showed improvement for modeled vorticity in each case. The calibration process that led to the determination of C_{opt} was performed by matching to a single streamwise vorticity core on a flow-normal crossplane. Although the model fit to that variable was much improved under those conditions, no additional validation of the use of C_{opt} under different flow conditions or on other variables or in other regions of the flow has been done. Further investigation of this same flow problem was performed

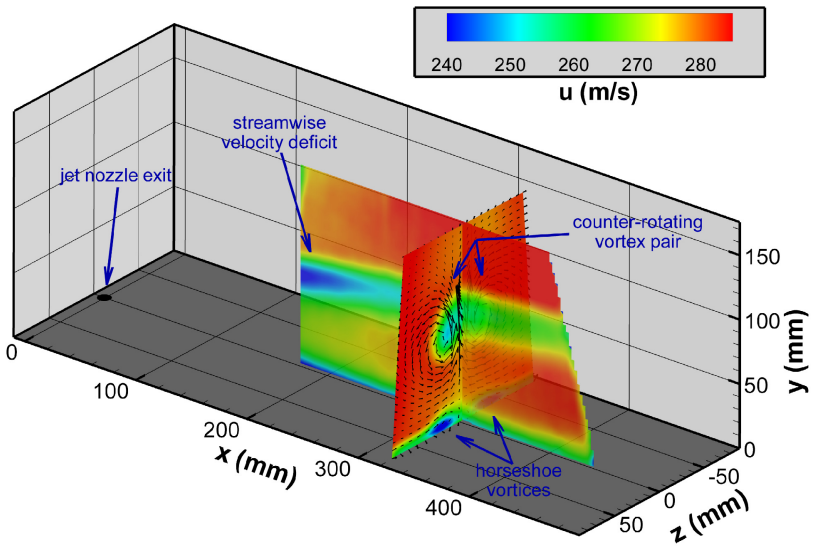

Fig. 1 Schematic of the TWT and mean JIC flow topology depicted using PIV data from Beresh et al. [32, 33] and collected on the x-y centerplane and a y-z crossplane at $x = 321.8$ mm. Reprinted with permission from Ray et al. [34].

analytically in DeChant et al. [28] and using similar PIV data in Miller and Beresh [29]. Both of those works found optimal values for C_μ (the primary component of C_{opt}) for this problem that were similar to the value recommended by Ray et al. [25].

This work is an effort to take C_{opt}, as determined by matching to $\overline{\omega}$ at a single location, and validate its usefulness in improving RANS predictions of multiple flow variables throughout the domain under a variety of flow characteristics. Thus, the validation domain has been expanded to fill a much larger portion of the operational envelope of transonic JIC by utilizing data from additional validation experiments [30]. The list of validated system response quantities (SRQs) of interest is also expanded from only vorticity in a single vortex core to include both $\overline{V_y}$ and $\overline{\omega}$ fields over entire PIV planes. In addition, the jet configuration is also modified to include canted jets. A series of validation metrics are presented and used to quantify the improvements (or lack thereof) to SRQ predictions when switching from the nominal parameters to those determined as optimal.

To that end, RANS simulations were run for a large number of JIC flows using both the nominal and optimal model parameters. The SRQs of interest were extracted from the converged results and comparisons were made to PIV data. A large set of PIV data collected over many years at Sandia National Laboratories (SNL) was tapped to provide the experimental data needed for the validation (Sect. II). The set of utilized metrics, each specifically chosen to give a different measure of the quality of the simulation results, compared both the nominal and optimal RANS solutions to the experimental data (Sect. III). The list of metrics includes some that measure the “global" fit as well as others that specifically track and measure the vortex cores in the CVP. Side-by-side comparisons of the RANS results and PIV data, along with the values of the quality metrics for each variable on each plane for each case being investigated, are shown (Sect. IV). This includes cases that differ considerably from the single case used for the parameter calibration. The present work builds on the initial efforts of Miller et al. [31] but adds additional comparisons over what was reported there and uses additional quality metrics for comparisons of the CVPs.

II. Experiments and Data

A. PIV

PIV data from multiple experimental campaigns, performed in different wind tunnels with different equipment and geometries, are used here for validation. The first sets of data, against which the nominal and calibrated RANS simulations were tested, were collected in the Trisonic Wind Tunnel (TWT) at SNL and have been reported and used

Table 1 The planes of PIV data taken from each experimental combination of nozzle inclinations (α) and dynamic pressure ratios (J). Cases highlighted in bold are used to represent uncertainties in Figs. 6-7.

	J = 2.8	J = 5.6	J = 8.1	J = 10.2	J = 16.7
α = 0°:	x = 321.8 mm	x = 321.8 mm	x = 321.8 mm z = 0.0 mm	**x = 215 mm** **x = 321.8 mm** z = 0.0 mm	x = 321.8 mm
α = 15°:	x = 321.8 mm	**x = 321.8 mm**	x = 321.8 mm	x = 321.8 mm	x = 321.8 mm
α = 30°:	x = 321.8 mm	x = 321.8 mm	**x = 321.8 mm**	**x = 215 mm** x = 321.8 mm	x = 321.8 mm
α = 45°:	x = 321.8 mm	x = 321.8 mm	x = 321.8 mm	x = 321.8 mm	**x = 321.8 mm**

in a number of previous studies (e.g., [12, 32, 33, 35–37]). The data are all from jet-in-crossflow experiments, each consisting of a wall-mounted nozzle venting a supersonic jet into a subsonic (Mach 0.8) crossflow (Fig. 1). The TWT cross section is 305×305 mm and the tunnel was operated with a freestream velocity of 285±2 m/s. Four different jet nozzles were used for separate tests, each with a design Mach number of 3.7 at the centerline of the nozzle exit. The first was oriented normal to the tunnel floor and thus vented the jet perpendicularly into the subsonic crossflow. The additional nozzles were inclined laterally to the freestream direction at angles of $\alpha = 15°$, 30°, and 45° and thus vented the jet into the crossflow perpendicularly to the freestream but canted in the crossplane. The nozzle with $\alpha = 0°$ had a circular exit with a diameter of 9.53 mm. The inclined nozzles had elliptical exits that resulted from the design which was based on a conical nozzle being scarfed by the plane of the tunnel wall passing through the centerpoint of the exit plane of the normal conical nozzle. The jet-to-freestream total temperature ratio for each of the nozzles was 0.93, with some small variations based on ambient conditions. The freestream Reynolds number based on the circular nozzle exit diameter was approximately 2×10^5. Additional dimensions and nozzle exit properties can be found in Beresh et al. [36].

PIV datasets were collected during multiple experiments in the TWT with nozzles of each of the inclination angles and at five different jet-to-freestream dynamic pressure ratios (J). Across the different experiments, PIV images were collected using a mixture of two-component PIV and stereoscopic PIV procedures and were collected on three different two-dimensional (2D) planes within the tunnel. The first plane was the x-y centerplane, which was aligned with the nozzle center ($z = 0$) and extended from ≈ 226 to 350 mm downstream of the nozzle. Data were collected on the centerplane only with the $\alpha = 0°$ nozzle and only for $J = 8.1$ and $J = 10.2$ [37]. The second plane was a y-z crossplane positioned at $x = 215$ mm (22.6 jet diameters) and roughly centered around $z = 0$. Data were collected on this crossplane during experiments with both the $\alpha = 0°$ and $\alpha = 30°$ jet nozzles, both with $J = 10.2$ [35]. The final plane was also a y-z crossplane, but was positioned at $x = 321.8$ mm (33.8 jet diameters). It was at this downstream location that the data used in Ray et al. [25] were taken. The data they used were taken with the 0°-inclined nozzle operating at a dynamic pressure ratio of $J = 10.2$ and had been previously reported in Beresh et al. [33]. Herein, data that were collected on this crossplane for experiments using all four nozzles at J values of 2.8, 5.6, 8.1, 10.2, and 16.7 are used (Table 1). This is a combination of the datasets reported in Beresh et al. [33] and Beresh et al. [36]. For further details on the PIV systems, equipment, and procedures readers are referred to the cited works. Results presented herein are ensemble averages from at least 3000 snapshots of data on each plane.

The second set of data used here was collected during a different experimental campaign and was previously reported in Beresh et al. [12]. Those data were collected during experiments performed on a full-scale flight vehicle model in a production-scale wind tunnel under a variety of conditions and represent the most complex and flight-realistic data against which the calibrated RANS could be tested. The experiments were performed in the NASA Ames Unitary Plan Wind Tunnel which, with its 3.4×3.4 m cross section, was able to hold a 3.6 m long, full-scale reproduction of an axisymmetric flight vehicle with four aft fins. Two nozzles were mounted into the model surface at approximately the model's midsection and had a lateral inclination angle of 39.5° to the surface normal. The nozzles were considerably larger than those used in the TWT, with an effective nozzle diameter at the model surface plane of 38.2 mm. The nozzles were designed to produce a nominal Mach number at the centerline of the nozzle exit of 3.66 by utilizing high-pressure

room-temperature air which was supplied at up to 20 MPa at 18 kg/s through the mounting sting. Schematics, pictures, and further details on the model and nozzles can be found in Beresh et al. [12].

A variety of tests were performed during the experimental campaign, with different freestream Mach numbers, dynamic pressure ratios, and angles of attack. Only the baseline case from that campaign is used here because many more PIV samples were taken for that case, thus substantially lowering the measurement uncertainty. That case used a jet stagnation pressure of 2.83 MPa while the wind tunnel was operated at a freestream Mach number of 0.8 with a stagnation pressure of 33.5 kPa, resulting in a jet-to-freestream dynamic pressure ratio of $J = 16$ [12].

By using a traverse system mounted alongside the tunnel, PIV data were collected on a set of y-z planes at a range of x locations from 414 to 820 mm downstream of the nozzle center. Herein, data from only the $x = 414$ and 820 mm planes were used for comparisons to the RANS simulation data. Further details on the PIV system are left to the cited work [12].

These multiple experiments were planned and conducted with validation in mind and efforts were made to satisfy the highest quality expectations for such experiments [38, 39]. The data were processed using the DaVis software package using state-of-the-art techniques like those described in Beresh et al. [40] and much of the data here was reprocessed from the original images to make use of more recent interrogation algorithms. As reported in Beresh et al. [33] the collective uncertainties inherent in the PIV data collected at $x = 321$ mm equate to ±9, ±4, and ±6 m/s in $\overline{V_x}$, $\overline{V_y}$, and $\overline{V_z}$, respectively. Given the spatial resolution of the PIV data and data processing techniques used for determining $\overline{\omega}$, the uncertainties in the velocity components can be translated into an uncertainty in $\overline{\omega}$ following Sciacchitano and Wieneke [41]. For the majority of the data presented here, collected at $x = 321$ mm, this resulted in an uncertainty in $\overline{\omega}$ of approximately ±900 s^{-1} everywhere on the planes. The data collected at $x = 215$ mm has a lower uncertainty in the velocity components but was processed with a 75% overlap and had a tighter spatial resolution. These competing properties result in an uncertainty in $\overline{\omega}$ of approximately ±1000 s^{-1}. For the sake of simplicity a single uncertainty value of 950 s^{-1} was used for the vorticity and a single value of ±5 ms^{-1} was used for $\overline{V_y}$ in each dataset presented here. Although more precise uncertainty quantification with spatial variability has become available for PIV in recent years [42], these simplified estimates are sufficient for the present application. Monte Carlo techniques were used to propagate the uncertainties in $\overline{V_y}$ and $\overline{\omega}$ into the set of quality metrics used to compare these SRQs of interest. Further details on the metrics and the propagation of the uncertainties are discussed in Sect. III.

B. RANS

The RANS data, produced with both C_{nom} and C_{opt}, were generated using SNL's parallel compressible gas dynamics code, SIERRA/Aero. The specifics of the k-ϵ model that is utilized in SIERRA/Aero are described in So et al. [43], Brinkman et al. [44], and in the released user's theory manual [45]. The model uses three parameters, $\{C_\mu, C_{\epsilon 1}, C_{\epsilon 2}\}$. C_{nom} was defined as {0.09,1.43,1.92} for the model parameters, respectively, (see Brinkman et al. [44]) while C_{opt} was defined as {0.1025,1.416,2.099} as specified in Ray et al. [25]. The diffusion coefficients, σ_k and σ_ϵ, were not independently optimized in Ray et al. [25] and were held constant at default SIERRA/Aero values, 1.0 and 1.3, respectively, in both sets of RANS simulations. The turbulent Prandtl number was maintained at a constant value of 1.0 (the default in SIERRA Aero) while the gas Prandtl number was set as 0.72.

To simulate the experiments performed in the TWT, a multiblock structured mesh of ≈ 7.9 million grid cells was defined from ≈ 32.0 jet diameters upstream to ≈ 100 jet diameters downstream of the jet nozzle. The spanwise and wall-normal dimensions were defined to match those of the TWT, the nozzle geometry was resolved down to the stagnation chamber, and wall-normal grid stretching was applied at all wall surfaces. The entire mesh is point-matched. An O-H topology was used from the stagnation chamber through the nozzle and then turned to follow an expected jet trajectory down the tunnel to the exit of the domain (similarly to Grid 2 of Arunajatesan and McWherter-Payne [46]). The tunnel mesh uses an H topology upstream of the nozzle and a hybrid topology downstream that matches the tunnel H topology to the O-H topology along the jet trajectory. A previous grid refinement study on a subset of the cases studied here demonstrated that this resolution was at the threshold of the minimum required to provide reasonably converged results. The grid refinement study used six meshes ranging from higher (500, 62.5, and 18.6 million cells) to lower (2.34 and < 1 million cells) resolutions and it was determined that numerical variations in the SRQs of interest became insignificant at the chosen mesh level.

Simulations were run using each of the parameter sets (C_{nom} and C_{opt}) for each of the combinations of the nozzle inclination angles and dynamic pressure ratios. The inlet boundary condition was kept constant across all simulations and consisted of a plane of state variables taken from a precursor simulation of the full length of the TWT with no JIC or nozzle present. The precursor simulation was run with C_{nom}. Its use as an inlet condition did not produce any

observable issues within the simulations run with C_{opt} and though a minor difference in mean BL growth along the tunnel wall occurred between the domain inlet and the jet, the difference in the resulting BL thicknesses was below the grid resolution at $x = -10$ jet diameters. The outlet boundary conditions were based on pressure measurements taken in the TWT. The desired dynamic pressure ratios for the jet were generated by setting the stagnation chamber boundary condition. The simulations were run with a Roe flux scheme, were spatially second order with a weighted least square gradient method, and a stenciled van Albada limiter was applied. Local time stepping was used in an implicit first-order backward-difference time-advancement method. All walls were treated as adiabatic. After reaching convergence, fields of $\overline{V_y}$, $d\overline{V_z}/dy$, and $d\overline{V_y}/dz$ were extracted from each simulation and were interpolated onto the same grid-planes at which the PIV data were collected. The interpolated gradients were then combined to form ω.

For simulating the experiment of the flight vehicle model, a multiblock structured mesh of ≈ 25.7 million hex elements was defined that included the entire flight vehicle but with far field boundaries instead of including the wind tunnel test section walls. The CFD model geometry included the vehicle body, tail fins, and the two nozzles mounted into the model surface as defined in Beresh et al. [12]. Mesh convergence studies demonstrated that this mesh results in converged integrated forces and moments, though the farfield flow solution, away from the jet and CVP region, may not be fully grid-converged. Again the appropriate planes of data were extracted from the results of simulations run with each set of model parameters so that direct comparisons could be made to the PIV data.

III. Validation Methods

In order to quantitatively assess the quality of the improvement to the RANS solutions by switching from C_{nom} to C_{opt} a set of six metrics were used to measure the spatial and magnitude differences between the SRQs from the PIV and RANS datasets.

The first three metrics were used to measure the prediction accuracy of the primary vortex cores as the behavior of those cores and their development with downstream distance is of significant interest to the engineering community. The size, strength, and location of the primary vortices visible in both the PIV and RANS datasets for each case were determined for comparison. In most cases two primary vortices were clearly distinguishable, though in some of the cases with relatively low J and high α values, only a single core could be reasonably identified. Additionally, a few cases exhibited third or even fourth regions of high vorticity, but in all but one of such cases those cores were either not identifiable in all three datasets and/or crossed over an edge of the crossplane's domain and therefore their sizes could not be identified. The one exception to this was that three cores were identified in all three datasets on the $x = 414$ mm plane of the tests performed around the flight vehicle model. In all the remaining cases, the historically well-established two-vortex CVP was clearly identified.

In Beresh et al. [12], a threshold of $1/e$ ($\approx 37\%$) of the peak streamwise vorticity ($\overline{\omega} = (d\overline{V_z}/dy - d\overline{V_y}/dz)$) within each core was used to define the core's shape, prior to then extending that shape out to a zero vorticity threshold which defined the core's outer boundary. Similarly here, a threshold of $1/3$ of each core's peak value was chosen to identify the cores' shapes. This simple threshold definition, though not quite at the edge of the identifiable vorticity, proved most robust for both PIV and RANS results and across all flow conditions, and thereby it allowed a suitable common definition. Using this boundary, the core perimeter (P) was determined so that the outer size of the cores could be compared reliably without regard to circularity or aspect ratio. The strength of each core was then quantified as the total circulation (Γ) within each core by integrating $\overline{\omega}$ over the area within the boundary. Finally, the y and z location of the "center of circulation" of each core were then determined using a center-of-mass-type approach as,

$$[\overline{y}, \overline{z}] = \frac{1}{\Gamma} \int [y, z]\, \overline{\omega}\, dA. \tag{1}$$

Examples of what the use of this thresholding criteria looked like in practice, and the resulting values of $\overline{y}$ and $\overline{z}$, are discussed in Sect. IV and shown in Figs. 3, 4, and 5. In those figures, the black isolines and the '×'s denote the vortex core boundaries as defined by the $1/3$ threshold and the individual core centers of circulation, respectively.

To facilitate meaningful comparisons across a range of cases, normalized versions of P and Γ were employed as,

$$P^* = \frac{P_R}{P_P}, \tag{2}$$

and

$$\Gamma^* = \frac{\Gamma_R}{\Gamma_P}, \tag{3}$$

where the subscripts R and P represent values taken from the RANS and PIV data, respectively. The error in the location of each vortex core was normalized by defining the Euclidian distance between each PIV vortex core center location and the RANS derived core center locations divided by the core perimeter from the PIV as,

$$E^* = \frac{\sqrt{(\overline{y_P} - \overline{y_R})^2 + (\overline{z_P} - \overline{z_R})^2}}{P_P}. \tag{4}$$

If the RANS data is a perfect predictor of the PIV data then Γ^* and P^* will both be one and E^* will be zero. These three metrics are only defined based on the mean streamwise vorticity and therefore were not applied to the centerplane data or to any other variables.

Because these three metrics were only applied to $\overline{\omega}$, only the uncertainty in $\overline{\omega}$ needed to be propagated to these metrics via a Monte Carlo approach. For each plane of data, random uncertainties were sampled from a Gaussian distribution with a standard deviation of 475 s^{-1} (thus a two-sigma of 950 s^{-1} as defined above) and applied to every point in the plane. This was repeated 5000 times per vortex core and the resulting distributions of Γ_P and the centers of circulation were then used in the metric formulations to get resulting distributions of Γ^* and E^*. This approach was illogical for determining distributions of P_P and then P^*, as the randomness of the applied uncertainties resulted in chaotic perimeters that were always substantially longer than the nominal perimeter. Therefore a different technique was used by applying a randomly sampled uncertainty to each core's peak vorticity value, determining the new $1/3$ threshold, and then finding the perimeter based on that threshold. This still resulted in many unsatisfactory perimeter values because the $1/3$ threshold had already been chosen as the minimum value that worked well across all cases. Essentially the $1/3$ threshold of the original peak value placed the core perimeter so near the diffuse, 'flat' portion of the vorticity field that even small changes to the threshold value result in large changes in the identified perimeter. Regardless of this, the results are reported as calculated. From the three nondimensional distributions, a 95% confidence interval was taken and is represented by uncertainty bands in the figures in Sect. IV.E.

The other three quality metrics proposed and used here are somewhat similar to metrics used in environmental fluid dynamics studies for evaluating the accuracy of plume models [47] and have been used by others for comparing models to large experimental datasets (e.g., [48–50]). These three metrics each measure the accuracy of the modeled data in different ways and by including all of the data from the planes simultaneously, they provide a more rigorous bulk comparison than tracking only peak values or peak locations.

The first of the bulk metrics was the mean squared error normalized by the mean squared magnitude of the PIV data. This is defined as,

$$MSE = \frac{\left\langle (X_{P,i,j} - X_{R,i,j})^2 \right\rangle}{\left\langle X_{P,i,j}^2 \right\rangle}, \tag{5}$$

where X represents any given dependent variable, the subscripts R and P are as previously defined, i and j indicate individual points on a 2D plane, the $\langle\rangle$ represent an average taken over the 2D plane being tested, and MSE goes to zero for a perfect model fit. The normalization of the mean squared error was done to allow for direct comparisons of MSE across different flow variables which had differing orders of magnitude. Also note that anytime the MSE has a value > 1.0 it means that the error between the fields is greater (in a mean squared sense) than the magnitude of the PIV data.

Because of the squares, the MSE is heavily biased towards errors in the peak values. The mean squared error has been used extensively as a quality metric but has the flaw that it is susceptible to biases created by extreme events or outliers in experimental data, especially when those data cross multiple orders of magnitude [47]. Specifically, a few outlying points of large magnitude that produce large absolute errors but small relative errors can bias the MSE regardless of the quality of the fit over the remaining data in the domain.

To reduce this bias and quantify improvements while minimizing the effects of outliers, the second bulk metric used was the geometric mean of the errors normalized by the geometric mean of the magnitudes defined as,

$$GME = \frac{\exp\left[\left\langle \ln(|X_{P,i,j} - X_{R,i,j}|)\right\rangle\right]}{\exp\left[\left\langle \ln(|X_{P,i,j}|)\right\rangle\right]}. \tag{6}$$

By not using squares and by taking the mean of the model-to-experiment difference in logarithmic space, this metric reduces the bias toward errors at high magnitude points. In that way, the GME does a better job than the MSE when data cover multiple orders of magnitude; it minimizes the bias of smaller relative errors in large numbers swamping any

larger relative errors in smaller numbers*. GME can therefore be seen as a measure of how well the RANS performs at predicting values away from the most extreme-valued regions of the flow while MSE is a measure of how well the RANS predicts those peak values.

The final of the bulk metrics was the 2D correlation coefficient defined as,

$$corr = \frac{\sum_j \sum_i [(X_{P,i,j} - \langle X_P \rangle)(X_{R,i,j} - \langle X_R \rangle)]}{\sqrt{\sum_j \sum_i [(X_{P,i,j} - \langle X_P \rangle)^2] \sum_j \sum_i [(X_{R,i,j} - \langle X_R \rangle)^2]}}. \tag{7}$$

The 2D correlation can take values between -1.0 and 1.0 and represents a measure of the spatial alignment between the two datasets. The magnitudes of the RANS-predicted values are of no consequence to $corr$ and an ideal value of 1.0 is still possible if the RANS values are wrong everywhere but are proportionately high when the PIV values are high and are proportionately low when the PIV values are low. If $corr = 0$ it suggests that the RANS results are no better than a random number distribution.

As these three metrics were applied to both $\overline{V_y}$ and $\overline{\omega}$ on each of the planes, a Monte Carlo approach was used with both uncertainties. Again Gaussian distributions with two-sigma defined by the collective uncertainties defined in Sect. II.A were used to produce random fields that modulated the mean PIV data which were then used to produce distributions of MSE, GME, and $corr$. Due to the nature of the normalizations used for MSE and GME, the addition of any amount of noise to the mean fields results in those formulations returning values nearer to unity than when only the mean fields are used, i.e., adding the same noise to the PIV data in both the numerator and denominator results in the metrics trending towards one. In many cases, this effect was so dramatic that the values of MSE and GME found using the mean fields (i.e., zero added uncertainty) did not land within the 95% confidence interval that resulted from the Monte Carlo method. In those cases, when uncertainty bands are used to represent the confidence intervals in Sect. IV.E, the metric values determined based on the mean PIV data replaced the appropriate bound, thus meaning that the uncertainty bands represent a range with closer to 97.5% confidence. Those cases therefore appear with single-sided confidence intervals instead of two-sided bands (Fig. 7 in Sect. IV.E).

For $corr$, the addition of the random noise almost always makes the values worse (closer to 0). Given that the added uncertainties have zero correlation in space, this makes intuitive sense. When this effect led to the mean-field $corr$ being outside the 95% confidence interval from the Monte Carlo approach, we again replace the appropriate bound with the $corr$ value determined from the mean data and thus the bands depict an interval $\geq$ 95% confidence in each case.

IV. Results

Given that a total of 40 different RANS simulations were run for this work, and a total of 48 independent planes of data were taken to use for comparison to the PIV (Table 1), it is infeasible to show plots of even one variable from every plane. We therefore chose only four sets of contour plots to demonstrate the general impact that the use of C_{opt} had compared to C_{nom}, before then showing the changes in the validation metrics for all of the simulations/planes. Similarly, we also restricted ourselves to only making comparisons of $\overline{V_y}$ and $\overline{\omega}$ across all planes. These two variables were chosen for a variety of reasons, not the least of which was that they were available in all of the PIV and RANS datasets, unlike higher order statistics like the Reynolds stress, which was not fully resolved in some of the PIV. These were also the variables of interest to the researchers in the primary motivating works [13, 25] and therefore demonstrating modeling improvements here helps advance the story those researchers started.

A. Centerplane for $\alpha = 0°$ and $J = 10.2$

First, the wall-normal velocity ($\overline{V_y}$) has been used as an indicator of the location, strength, and spacing of the counter-rotating vortex pair (CVP) that typifies the JIC interaction [32]. This, combined with the fact that the streamwise vorticity could not be resolved on the streamwise-oriented centerplanes, meant that $\overline{V_y}$ was the only SRQ used for quantifying the accuracy of the RANS simulations on the centerplane. For the case where $\alpha = 0°$ and $J = 10.2$, the RANS simulation performed with C_{nom} significantly overestimated $\overline{V_y}$ on the centerplane. This result is also tied to the centerline of the jet core being farther from the wall and increasing its distance from the wall at a faster rate with

*This definition of GME should not be confused with the "geometric mean bias" defined in Chang and Hanna [47], which is undefined for a dependent variable with negative values.

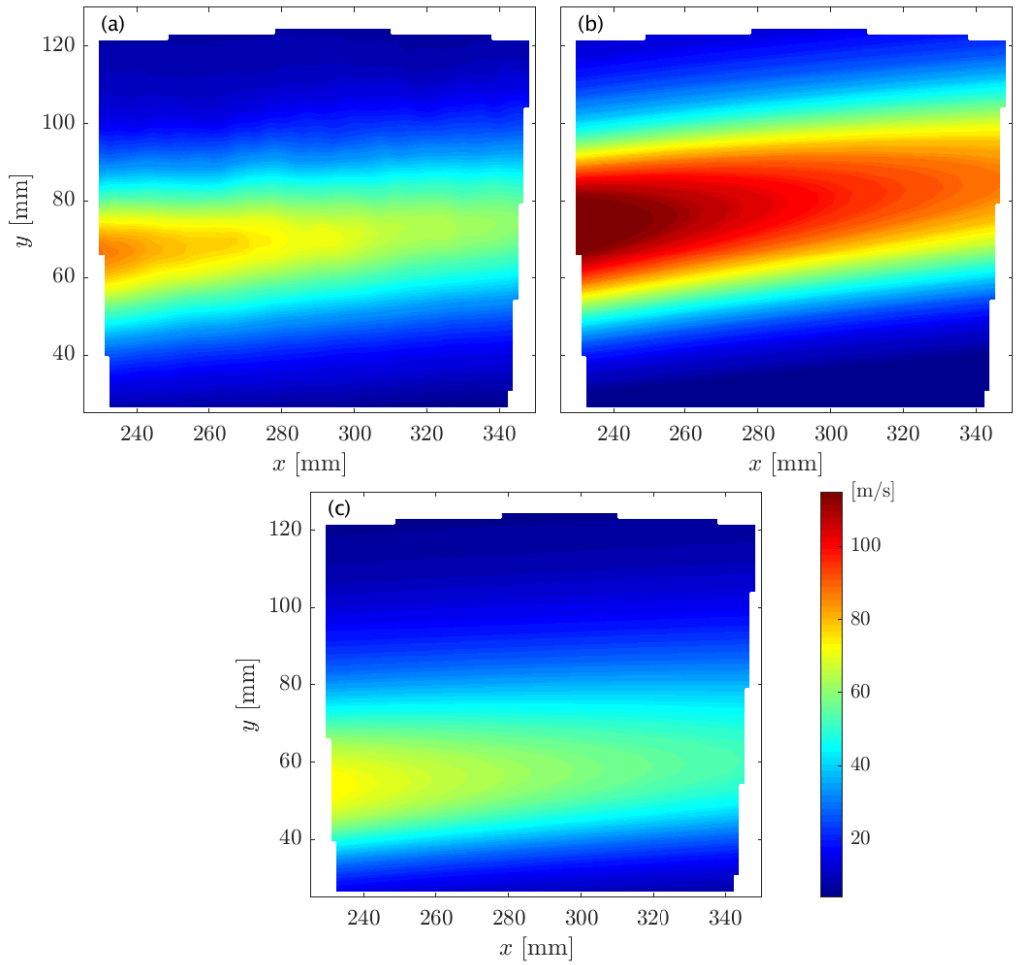

Fig. 2 $\overline{V_y}$ on the centerplane with $\alpha = 0°$ and $J = 10.2$. (a) the PIV data and the RANS data using (b) C_{nom} and (c) C_{opt}.

downwind distance than was observed in the PIV (Fig. 2). Conversely, when C_{opt} was used, the magnitude of $\overline{V_y}$ was considerably reduced, but was overcorrected somewhat resulting in the jet core being closer to the tunnel wall than was observed in the PIV.

Because the RANS result predicted by using C_{nom} was better aligned with the PIV data at the upstream edge of the domain and because the extents of the modeled jet were so much larger, thus overlapping the PIV data, that simulation achieved a slightly higher $corr$ than did the results predicted with C_{opt} (Table 2). The modeled jet based on C_{opt} had the jet centerline too close to the wall. However, because the magnitudes of $\overline{V_y}$ were consistently overpredicted throughout the core in the C_{nom} simulation, the MSE and GME values for that data were worse than those determined for the C_{opt}-derived results.

The magnitude of the $\overline{V_y}$ values is often an indicator of the strength of the circulation in the CVP that is drawing fluid up through the middle of the jet core. The higher $\overline{V_y}$ magnitudes observed when C_{nom} was used suggested that the CVP had a stronger vorticity magnitude and/or that the lateral separation between the counter-rotating cores was smaller than what was expected based on the PIV or what was seen when C_{opt} was used. This is explored in the following section by examining plots of the streamwise vorticity field.

B. Crossplanes for $\alpha = 0°$ and $J = 10.2$

For the case where $\alpha = 0°$, $J = 10.2$, and on the $x = 215$ mm plane, the RANS solution using C_{nom} does indeed show CVP core vorticities that are stronger than were observed in the PIV and that the cores are farther from the wall

Table 2 Quality metrics for $\overline{V_y}$ on the centerplane as depicted in Fig. 2.

	MSE	GME	$corr$
C_{nom}	0.506	0.575	0.802
C_{opt}	0.119	0.306	0.789

and closer together (Fig. 3). This is consistent with the nominal results shown in both Arunajatesan [13] and Ray et al. [25]. The cores' boundaries and centers are denoted in the figure by the black isolines and '×'s, respectively, following the definitions given in Sect. III.

The use of C_{opt} resulted in a lowering of the location of the CVP cores and a reduction in the strength of the vorticity. But, as with $\overline{V_y}$, the correction may have been too large as the cores moved closer to the wall than was seen in the PIV. This again led to the C_{nom}-derived data having a better $corr$ value than did the C_{opt}-derived data (Table 3). Similarly, the movement of the core centers towards the wall improved E^*_- but made E^*_+ worse, where the subscripts indicate the negatively- and positively-oriented cores, respectively. The correction in the strength of the vorticity in the CVP cores by using C_{opt} did result in better Γ^*s and a reduction in MSE, but the value of GME was actually slightly worsened. This suggests that although the most extreme vorticity values in the CVP cores were more accurate while using C_{opt}, moderate vorticity values elsewhere in the crossplane may have been made slightly worse, a result that may also be tied to the issue with the spatial alignment.

These results are particularly interesting because Ray et al. [25] used this exact variable ($\overline{\omega}$) from this exact case for determining C_{opt}, but the data used there were only of the negatively-oriented vortex core and were from the plane at $x = 321.8$ mm. When the quality metrics for that plane were investigated, $corr$, MSE, and GME indeed improved with C_{opt} and the location and strength of the negatively-oriented core were also more accurate (Table 3). This may suggest that in correcting the location and magnitude of the vorticity at $x = 321.8$ mm, the calibration overcorrected the location and intensity at $x = 215$ mm. This would in turn suggest that there is some other issue causing the trajectory of the jet core to be incorrect, such that it overshoots the right location at $x = 321.8$ mm when it is correct at 215 mm or undershoots the correct location at $x = 215$ mm when correct at 321.8 mm. Surprisingly, these metrics from the $x = 215$ mm crossplane constitute arguably the worst result that was seen among all of the sets of quality metrics calculated (can be seen as the black stars on the wrong side of the lines in Figs. 7(b) and (c) later). For every other set of comparisons, the metrics were collectively better.

An additional factor that may be contributing to the poorer metric behavior for this case is the visible asymmetry in what is a nominally symmetric flow configuration. Slight asymmetries in both the shapes and magnitudes of the cores are observable in the experimental data and these may not be replicated by the simulations. Beresh et al. [33] suggested that the experimental asymmetry may be credited to imperceptible asymmetries in the nozzle, below machining tolerance, or in the tunnel freestream. Other experiments have shown similar results, leading to speculation that the jet-in-crossflow may be an inherently asymmetric flow [7], perhaps due to convective instabilities [51] and possibly as a function of flow parameters like Mach number, Reynolds number, and J [52]. Similarly asymmetries also appear in the simulated data, both here and in the simulations of Arunajatesan [13], which were performed with different turbulence closure models and with a different CFD solver than was used here. Given that unsteadiness is not believed to be a factor in the included simulations, the cause for the asymmetry may be attributable to the same inherent instabilities observed in the experimental data and/or numerical instabilities or meshing discrepancies that lead to more extreme asymmetries than are physical or observed in the experiments. While the asymmetric phenomena do add complexity to the comparisons of the experimental and simulated data, the only cases for which the quality metrics may be affected are those where $\alpha = 0°$. Regardless of this, the metrics show general improvements even when $\alpha = 0°$ and often show even greater improvements when the nozzle is inclined.

C. Crossplanes for $\alpha = 30°$ and $J = 10.2$

A much more noticeable improvement in the RANS solution based on C_{opt} was seen for the case when $\alpha = 30°$ and the data were taken at $x = 215$mm with $J = 10.2$ (Fig. 4). These data were not used in determining C_{opt}, were taken from a somewhat more complicated flow, and were taken at a different downstream location than were the data used for determining C_{opt}. These data are also more closely representative of a flight application of interest [12]. Both the general shape of the vorticity field and the magnitudes of the vorticity within the individual cores were improved with

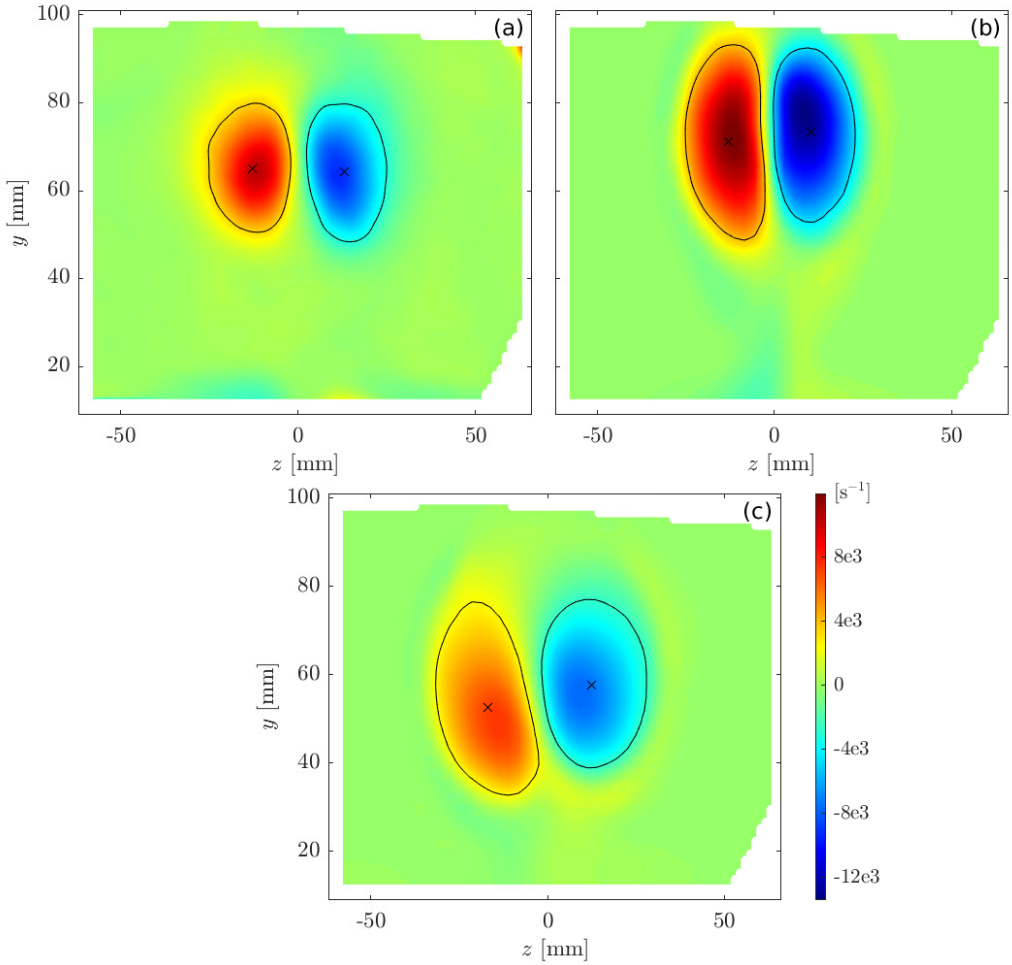

Fig. 3 $\overline{\omega}$ **on the crossplane at** $x = 215$ **mm with** $\alpha = 0°$ **and** $J = 10.2$**. (a) the PIV data and the RANS data using (b)** C_{nom} **and (c)** C_{opt}**.**

Table 3 Quality metrics for $\overline{\omega}$ **as depicted in Fig. 3 and as taken from the** $x = 321.8$ **mm plane of the same case.**

		MSE	GME	$corr$	P^*_-, P^*_+	Γ^*_-, Γ^*_+	E^*_-, E^*_+
$x = 215$ mm:	C_{nom}	0.761	1.06	0.838	1.17,1.31	1.89,1.82	0.109,0.074
	C_{opt}	0.556	1.12	0.716	1.24,1.37	1.34,1.25	0.080,0.157
$x = 321.8$ mm:	C_{nom}	1.789	1.12	0.684	1.12,1.15	2.12,2.04	0.159,0.105
	C_{opt}	0.672	1.06	0.715	1.22,1.21	1.48,1.42	0.060,0.132

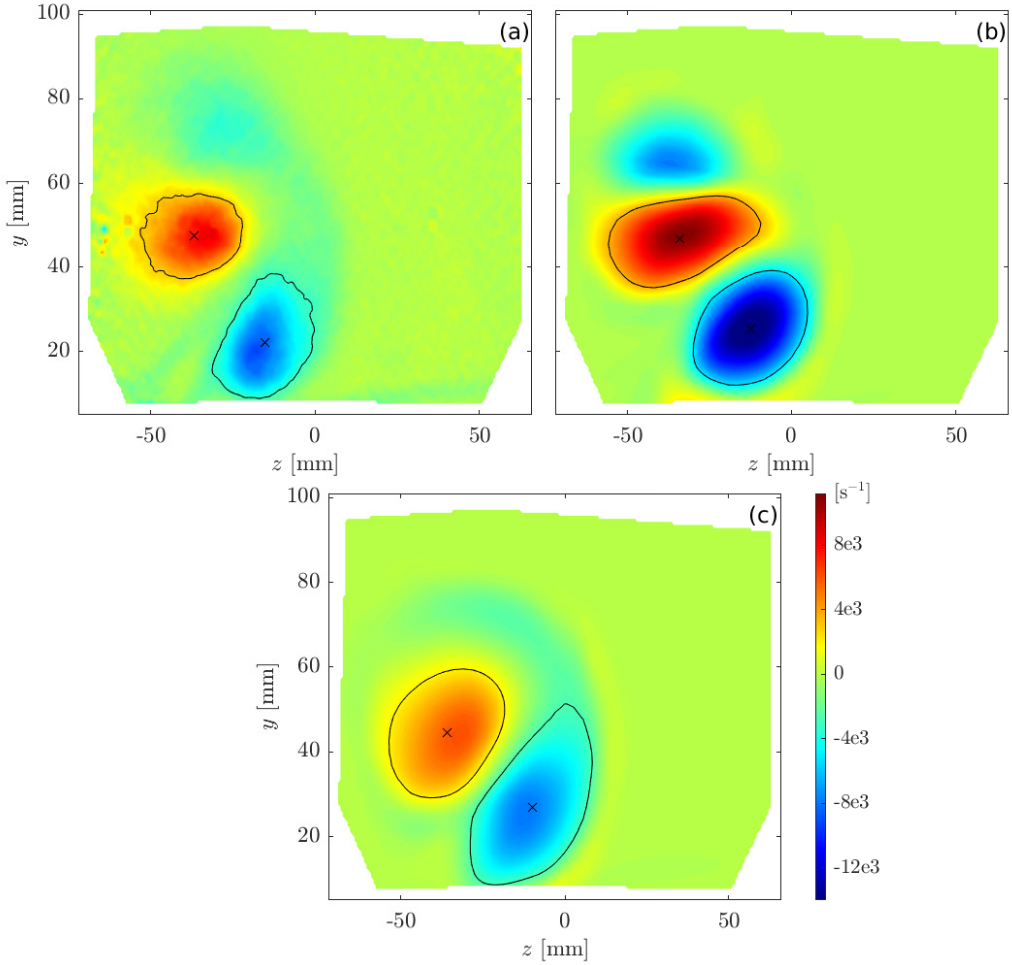

Fig. 4 The same as Fig. 3 but with $\alpha = 30°$.

Table 4 Quality metrics for $\overline{\omega}$ as depicted in Fig. 4 and as taken at the x = 321.8 mm plane of the same case.

		MSE	GME	$corr$	P^*_-, P^*_+	Γ^*_-, Γ^*_+	E^*_-, E^*_+
x = 215 mm:	C_{nom}	0.987	1.00	0.853	1.02,1.27	2.00,2.06	0.047,0.034
	C_{opt}	0.210	0.78	0.894	1.30,1.19	1.50,1.25	0.076,0.038
x = 321.8 mm:	C_{nom}	1.393	1.07	0.830	1.05,1.23	2.17,2.09	0.043,0.039
	C_{opt}	0.198	0.82	0.911	1.36,1.02	1.53,1.24	0.063,0.014

the use of C_{opt}. When the improvements seen by using C_{opt} were quantified using the quality metrics, all three bulk metrics reflected these qualitative observations by showing the C_{opt}-derived results to be a significant improvement over the C_{nom} results (Table 4).

In contrast, when looking at the individual vortex cores, P^* and E^* did not show the same improvement with the use of C_{opt}. For both vorticity cores E^* became slightly worse, while P^* became worse for only the negatively-oriented vortex. This can be seen in the figure, as the use of C_{opt} made the negative core slightly too large and moved the core centers to be slightly misaligned. The larger boundary is a result of the simulated cores having lower peak magnitudes than seen in the PIV or when C_{nom} was used, thus resulting in lower magnitude thresholds for defining the core boundary shapes, thereby making the cores larger. Those lower magnitudes were closer to the PIV values than were seen when C_{nom} was used (thus the improved MSE), but for the negatively-oriented core specifically, result in the identified core boundary being more diffuse than in the PIV. If, by contrast, the peak values from the PIV cores were used to define the threshold for the shapes in all three datasets—instead of using the peak core magnitudes from the individual simulated cores—it would reduce the size of the cores in the C_{opt} results and increase the size of the cores in the C_{nom} results. This would improve the P^* value for C_{opt} while making P^* worse for C_{nom}. At the same time, this would likely worsen Γ^* for both RANS datasets. Using such a definition would therefore produce more impressive quality metric improvements for this case, but in many other cases it does not produce usable results because core boundaries were often no longer coherent or smooth, or were so vanishingly small as to make them unusable.

At the x = 321.8 mm plane for this same case ($\alpha = 30°$ with J = 10.2), similar results were seen in the quality metrics (Table 4). Specifically, Γ^*, $corr$, MSE, and GME all showed marked improvements when C_{opt} was used, while P^* and E^* showed more mixed results. Based on both P^* and E^*, the negatively-oriented vortex location and shape were predicted slightly less accurately, while the positively-oriented vortex shape and location were better predicted.

D. Crossplanes for the flight vehicle model

One of the most rigorous tests of the calibrated k-ϵ parameters was comparisons made to the data taken in the vicinity of the full-scale flight vehicle model. Given the cylindrical coordinate system of the vehicle and the clocking position of the jet nozzles on the vehicle body, velocities and gradients were defined based on the orientation of the vehicle in the wind tunnel and are therefore not specifically aligned with the nozzle exit normal as they were in the TWT. Direct comparisons were then made for both $\overline{\omega}$ and $\overline{V_y}$ (where y is normal to the tunnel floor [12]) between the RANS and PIV data. Contours for $\overline{\omega}$ at x = 820 mm showed that the k-ϵ model with both sets of parameters was able to generate the correct general flow topology (Fig. 5). Use of C_{nom} resulted in vortex cores with higher vorticity magnitudes and produced a second negatively-oriented vortex core near the top of the domain window defined by the PIV. The use of C_{opt} resulted in lower vorticity magnitudes than both the PIV and the C_{nom}-derived results, but they were more accurate than the C_{nom}-derived magnitudes (leading to better Γ^* and MSE). C_{opt} also clearly produced a better spatial alignment to the PIV data than did the use of C_{nom}, which also resulted in an improved $corr$. In fact, MSE, GME, and $corr$ were all improved for $\overline{\omega}$ when C_{opt} was used (Table 5). This was also the case on the other investigated plane (at x = 414 mm) and for $\overline{V_y}$ on both of the planes.

When looking at the vortex core metrics, again the use of C_{opt} showed general improvements. On the x = 820 mm plane, the locations of the core centers were both improved and the total circulation was more accurate within each core. For the negatively-oriented core specifically, the use of C_{nom} produced a perimeter that was smaller than was seen in the PIV while the use of C_{opt} produced a perimeter larger than the PIV. This is again attributed to the slight overcorrection of the use of C_{opt} leading to more diffuse core boundaries. Technically the smaller core (from C_{nom}) has a perimeter more similar to the PIV size but the difference is minimal. A similar result was observed on the x = 414

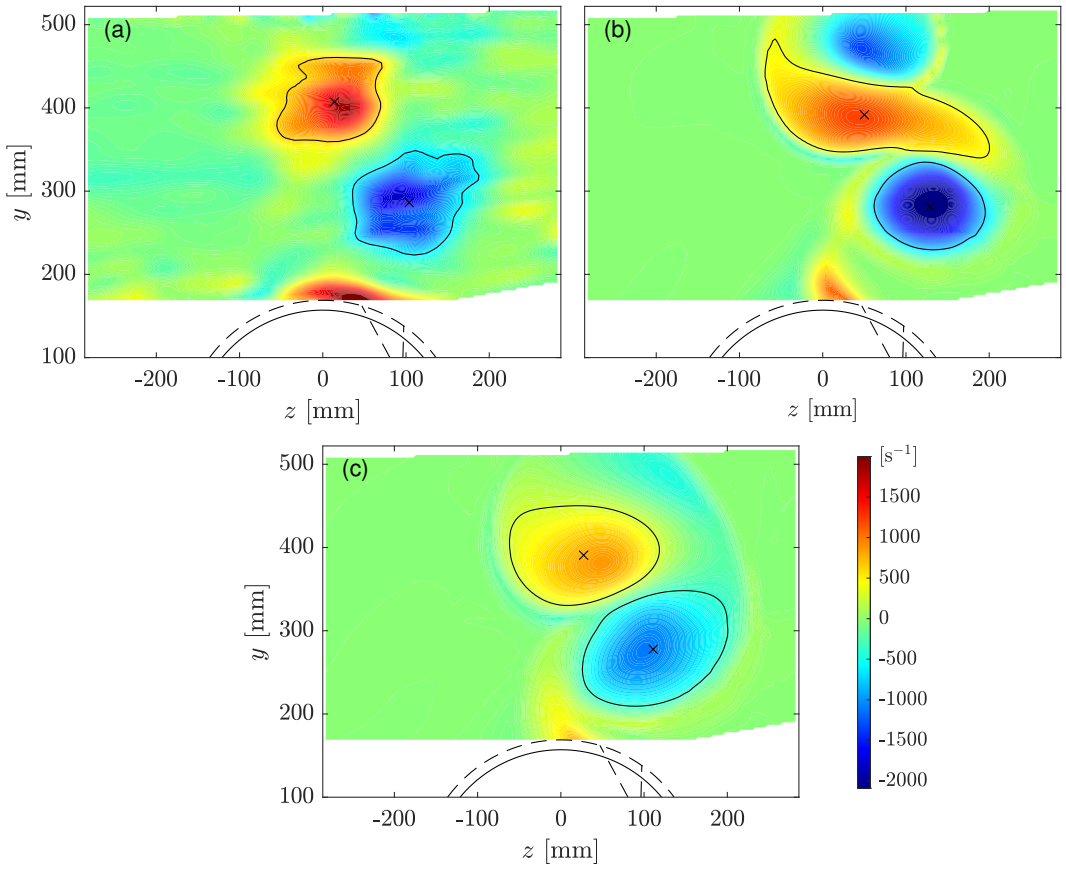

Fig. 5 $\overline{\omega}$ at x = 820 mm as viewed aft from the flight vehicle nose. (a) the PIV data and the RANS data using (b) C_{nom} and (c) C_{opt}. The dashed and solid arcs depict the vehicle's surface at the x locations of the nozzles (also shown as dashed lines) and of the PIV plane, respectively.

mm plane, in that the negatively-oriented vortex core nearest to the vehicle became larger when C_{opt} was used than was seen in the PIV, leading to a slightly worse P^* even though the total circulation and core location were improved. Recall that for the x = 414 mm plane, three vortex cores, including two that were negatively oriented, were identified and compared. In Table 5, the metric results for the negatively-oriented cores are listed first, followed by the metrics for the positively-oriented cores. In this case, nearly all the metrics of comparison were substantially improved by use of C_{opt} vs C_{nom} despite the numerous differences between the flight vehicle case and the small-scale unit problem used for calibration.

E. Collective Quality Metric Behavior

For the sake of brevity, no additional sets of contour plots are shown, but the quality metrics are assessed across all of the comparable datasets. Looking at the three metrics based on the strength, size, and location of the vortex cores, plots of the metric values show that while vortex circulation strengths were universally improved by using C_{opt}, the story of the vortex sizes and locations was somewhat more complex (Fig. 6). There were 24 planes of data taken from the TWT and the RANS solutions using each C_{nom} and C_{opt} but as the streamwise vorticity was not studied for the two centerplanes, only 22 planes of data were used for these metrics. There were two additional planes on which comparisons were made to the PIV data taken in the vicinity of the full-scale flight vehicle model tested in the tunnel at NASA, Ames. These planes resulted in a total of 44 identified cores for which metric comparisons could be made, i.e., five planes exhibited a single identifiable core for comparison while 18 had two and the x = 414 mm plane of the flight vehicle had three.

By plotting $|1 - \Gamma^*|$, values closer to zero indicate improved performance when using C_{opt}, and thus points that land below the 1-to-1 line (Fig. 6(a)) show an improvement in the simulated vortex strengths when C_{opt} was used. For all

Table 5 Quality metrics for $\overline{V_y}$ and $\overline{\omega}$ on the planes collected in the vicinity of the full-scale flight vehicle.

			MSE	GME	$corr$	P^*_-, P^*_+	Γ^*_-, Γ^*_+	E^*_-, E^*_+
$\overline{V_y}$:	x = 414 mm:	C_{nom}	1.64	1.23	0.291	–	–	–
		C_{opt}	1.25	1.20	0.389	–	–	–
	x = 820 mm:	C_{nom}	1.18	0.905	0.633	–	–	–
		C_{opt}	0.564	0.647	0.764	–	–	–
$\overline{\omega}$:	x = 414 mm:	C_{nom}	3.636	1.28	0.487	1.07,0.95,2.09	3.15,1.96,3.17	0.275,0.109,0.178
		C_{opt}	1.688	1.20	0.494	1.05,1.12,1.51	1.63,1.82,2.03	0.226,0.108,0.188
	x = 820 mm:	C_{nom}	0.787	1.01	0.660	0.82,1.72	2.22,2.78	0.056,0.096
		C_{opt}	0.273	0.78	0.866	1.10,1.20	1.86,1.75	0.024,0.052

44 of the comparisons done here, the integrated strengths of the circulation within each of the vortex cores improved when C_{opt} was used instead of C_{nom}. The impact of this result cannot be understated. The calibrated coefficients were determined based on a single vortex core on a single plane of data from a single flow configuration and yet those coefficients improve the accuracy of the amount of circulation in all 44 cores taken from the variety of flow configurations and planes studied here.

Uncertainty bands, used to denote the confidence interval of the Monte Carlo uncertainty propagation, are included for a subset of the 44 available cores. The cores chosen are those from the cases listed in bold in Table 1. These are representative of the breadth of uncertainty propagation results seen across all the cases. As can be seen in Fig. 6(a), none of the depicted intervals cross the 1-to-1 line. Including uncertainty bounds for all 44 vortex cores would have made the figure unreadable, but would have shown that only one core had intervals cross the 1-to-1 while the remaining 43 do not cross that line within the 95% confidence.

As promising as this result is, it is tempered somewhat by the behavior of the metric P^*. The figure depicts $|1 - P^*|$ for each core from the simulated datasets so that points below the 1-to-1 line again show improvements when C_{opt} was used instead of C_{nom}. An improvement in the vortex perimeters was observed in 17 of the identified vortices. The use of C_{opt} seemed to consistently produce vortex cores with lower peak vorticity values than did using C_{nom}. This was generally an improvement in the simulated results as the PIV values were typically lower than those estimated using C_{nom}, but often the correction was too large and then under-predicted the PIV peaks. The differences in the peak values lead to different thresholds for defining the core boundaries, which consistently made the cores larger and more diffuse in the C_{opt}-derived results than in the PIV. This seems to have particularly been a problem for the negatively-oriented vortex cores which were close to the wall in each of the cases with inclined nozzles. As shown above, for the case with $\alpha = 30°$ and $J = 10.2$ (Fig. 4), the negatively-oriented core is nearer to the wall, and in the C_{opt}-derived results is larger and more diffuse than in the PIV. So even when the positively-oriented cores' P^*'s are improved, and although Γ^*'s are improved for the negatively-oriented cores, the perimeters of those cores become larger than expected (Table 4). Negatively-oriented cores account for 19 of the cores for which P^* was not improved, with 14 of those coming from cases with inclined nozzles.

As explained in Sect. III, the individual core perimeters were very sensitive to the added uncertainty on the vorticity. In large part this was because the $1/3$ threshold used for defining the perimeter was chosen as low as it could be while still producing logical core bounds in all of the cases. As a result, large changes in the perimeter for even moderate amounts of uncertainty cause confidence intervals in $|1 - P^*|$ to be on the order of $|1 - P^*|$ itself. Thus, for most of the vortex cores, the intervals reach across the 1-to-1 line and therefore obscure whether P^* truly is improved or not. Of all of the core perimeters, only eight possess uncertainties that did not reach across the 1-to-1 line, and each of these were negatively oriented and came from cases with inclined nozzles. This is depicted for both the $\alpha = 30°$, $J = 10.2$ and $\alpha = 45°$, $J = 16.7$ cases (Fig. 6(b)) for which the uncertainty bands do not cross.

The final of the three core-based quality metrics was E^*, which should approach zero for a perfect simulation result. Thus, again, points below the 1-to-1 line (in Fig. 6(c)) indicate a more accurate result when C_{opt} was used than when C_{nom} was used. The locations of the vortex core centers were improved for 30 of the 44 identified cores. Additionally, the average improvement in E^*, for the cores that showed improvement, was more significant than the average worsening in E^* for the 14 cores where C_{nom} was better. Specifically, using C_{opt} improved the 30 superior core locations by

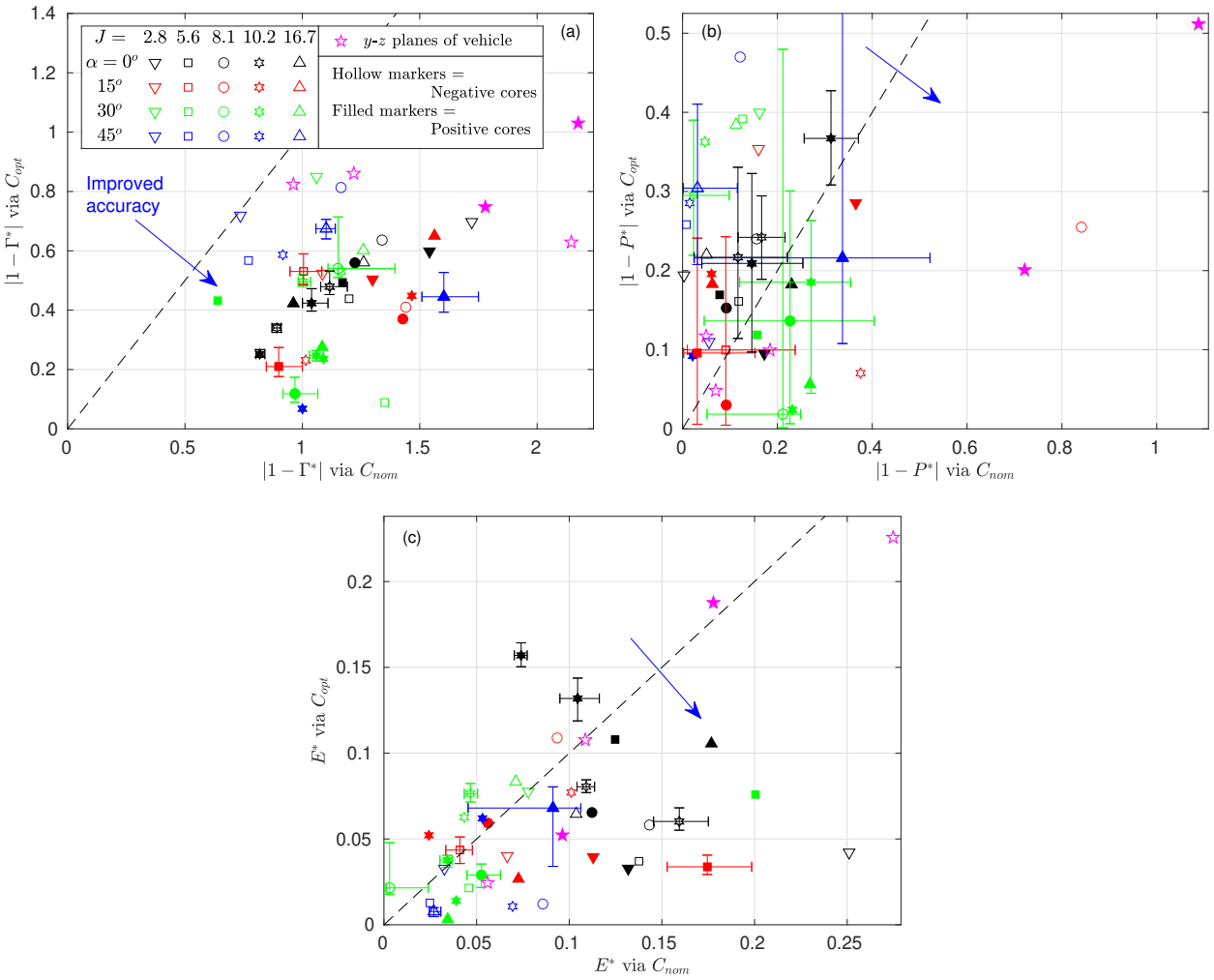

Fig. 6 The quality metrics of the vortex cores comparing the RANS to the PIV data. (a) Γ^*, (b) P^*, and (c) E^* for C_{nom} and C_{opt}.

an average of 5.5% of their respective perimeters, i.e., their values are 0.055 below the 1-to-1 line on average. The remaining 14 cores were worsened by only 1.9%, on average, when C_{opt} was used. Of the cores that showed the largest worsening of E^*, two of them were again from the $\alpha = 0°$, $J = 10.2$ case, the alignment of which was discussed above (Sect. IV.B). Overall, E^* indicates a substantial, though not universal, improvement in vortex simulation when C_{opt} is used.

Considering all of the confidence intervals on E^*, in the best case, eight of the bands reached across the 1-to-1 line to the improved side, resulting in a maximum of 38 cores for which E^* was improved with C_{opt}. In the worst possible case, only six of the identified cores have confidence intervals that reached from the region of improvement to the worse side when C_{opt} was used, resulting in a maximum of only 20 of the 44 core E^*s that may have been worsened by switching parameters.

One final point, that is not captured well within these metrics, is that the general shapes of the cores appears to have improved with the use of C_{opt}. This is quite visible in the positively-oriented vortex depicted in Fig. 5. This sometimes occurred at the expense of a slightly less accurate core center location, but it appears obvious which of the simulated cores is "more correct" in the figure, even if the center of the core is slightly less accurate with C_{opt}. Visual inspection of all cases finds that this is a common trend.

Moving on to comparisons of the three bulk metrics, 50 total comparisons were made between the data determined from RANS using the two different sets of parameters and PIV data (Fig. 7). These came from the 24 planes of data taken in the TWT and the two additional planes taken in the vicinity of the full-scale flight vehicle model, and the fact

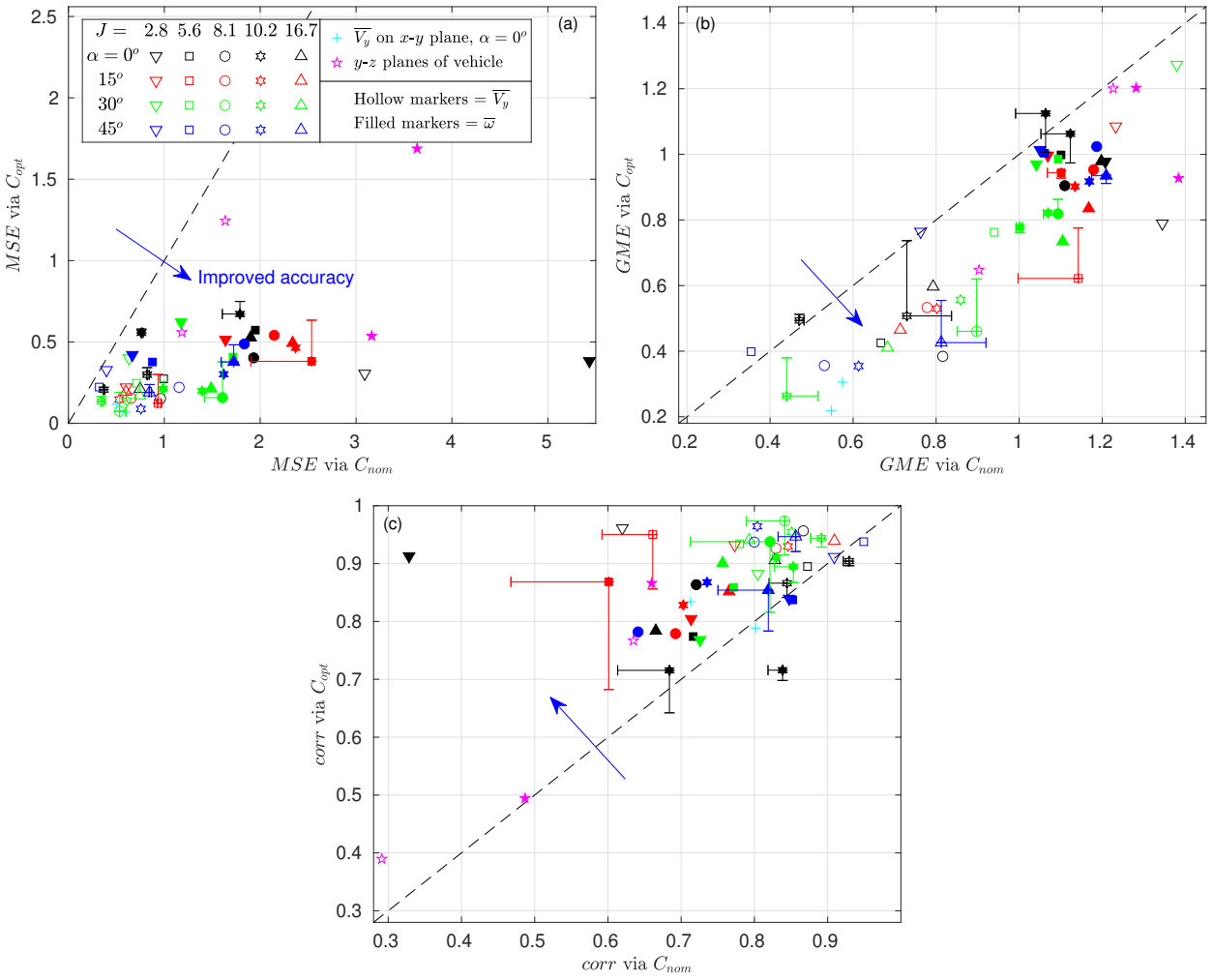

Fig. 7 The bulk quality metrics comparing the RANS using C_{nom} and C_{opt} to the PIV data. (a) MSE, (b) GME, and (c) $corr$.

that two variables, $\overline{V_y}$ and $\overline{\omega}$ were compared—though the streamwise vorticity was not calculated on the centerplanes.

The MSE values determined when comparing the PIV data to the RANS solution using C_{opt} were lower (better) than the MSEs determined based on C_{nom} in every one of the 50 comparisons (Fig. 7(a)). This is a strong indication that the use of C_{opt} is a general improvement over using C_{nom} for these jet-in-crossflow experiments, regardless of the specific flow case. Using C_{opt} produced more accurate peak velocity and vorticity values than did C_{nom} in every case. Again the impact of this result cannot be understated. A small change in the model parameters to a set defined as optimal for a single transonic JIC case improved the measured squared error in every other case tested.

It also appears that the improvement in MSE is somewhat more pronounced for the $\alpha = 0°$ and 15° cases than for the other inclination angles. This may be related to the fact that as α increases, the vortex cores stay closer to the wall and are increasingly tied to the boundary layer and HSV flow. This results in a merging of the vortical structures with the wall-bounded features outside of the PIV frame and therefore fewer visible features to be modeled within the window [36]. The simpler visible flow fields of the cases with the higher nozzle inclination angles had less room for improvement than did the cases with the lower angles. C_{nom} already performed relatively well for these cases. It may also be related to the fact that the $\alpha = 0°$ and 15° cases are the most similar to the case used for the calibration procedure that resulted in the determination of C_{opt}. The cases with the steeper inclination angles (and with the lowest Js) were the most different from the calibration case and therefore constitute a more extreme test of the applicability of C_{opt}.

Additionally, it appears that the improvements in the predictions of $\overline{\omega}$ were more significant than the improvements in predictions of $\overline{V_y}$. When considered collectively, the MSE values for $\overline{\omega}$ were lowered by 71% on average when

C_{opt} was used. The predictions for $\overline{V_y}$ already had lower MSE values than did $\overline{\omega}$ when using C_{nom} but still showed improvement of 65% when C_{opt} was used.

Uncertainty bands were again used to depict the confidence intervals that came out of the Monte Carlo uncertainty propagation and again only the same subset of the available cases are shown so as not to clutter the figures. Although none of the bands chosen for depiction crossed the 1-to-1 line, a total of five confidence intervals of MSE crossed the 1-to-1 line, suggesting that for only those five cases, the probability of improvement by using of C_{opt} was less than 95%. The rarity of the uncertainty bands crossing the 1-to-1 line suggests improvement in MSE was nearly universal when using C_{opt}. Interestingly, all five of the points which had confidence intervals cross the line were from cases where the vortex structures sat very near the wall (low J and high α).

Investigation of the GME results showed a similar, though slightly less dramatic result than MSE (Fig. 7(b)). In 46 of the 50 comparisons, the RANS results based on C_{opt} produced a better GME measure than did the results based on C_{nom}. Because GME is a measure of how well the model does at predicting values away from the most extreme-valued regions, this result suggests that not only does the use of C_{opt} improve the predictions of peak values of the investigated variables, but also does better at predicting those variables around the edges of the core regions and in the freestream. The four comparisons where the nominal approach remained slightly better than the calibrated approach were two comparisons of $\overline{V_y}$ on planes at $x = 321.8$ mm with $\alpha = 45°$ and $J = 2.8$ and 5.6, the comparison of the streamwise vorticity as discussed above (Table 3), and the comparison of $\overline{V_y}$ at $x = 215$ mm from that same $\alpha = 0°$, $J = 10.2$ case.

Contour plots of the mean velocities from the PIV for the cases with $\alpha = 45°$ and $J = 2.8$ and 5.6 can be found in Beresh et al. [36], and show the relative simplicity of the visible flow topology for those cases as mentioned above. The use of C_{opt} reduced the peak velocity magnitudes correctly, resulting in the improved MSE values, but resulted in CVP cores that were more laterally inclined than in the PIV or C_{nom} simulations. This inclination resulted in poor alignment of velocity values around the edges of the CVP cores, leading to slightly elevated GME values. These two cases were arguably the most different from the case used in determining C_{opt}. For the case with $J = 5.6$, this incorrect inclination of the vortex cores also resulted in a poorer $corr$ value, discussed next. The confidence intervals on these two cases did reach back across the 1-to-1 line, meaning, that along with the vorticity for the $\alpha = 0°$, $J = 10.2$ case (Fig. 7(b)) 49 of the 50 studied planes may have had improved GME values when using C_{opt}. The confidence intervals also suggest, that in the worst possible case, as many as 11 planes may not have been improved by using C_{opt}.

The $corr$ value based on $\overline{V_y}$ for the $J = 5.6$, $\alpha = 45°$ case was one of only six comparisons, from among the 50, where the correlation coefficient was slightly worse when C_{opt} was used instead of C_{nom} (Fig. 7(c)). The remaining five comparisons where C_{nom} produced superior $corr$ values were the comparisons of $\overline{\omega}$ taken from the same two $\alpha = 45°$ cases for which the GME of $\overline{V_y}$ was also worsened, the comparison of vorticity for the $\alpha = 0°$ case discussed above (Table 3), the comparison of $\overline{V_y}$ for that same $\alpha = 0°$, $J = 10.2$ case, and the comparison of $\overline{V_y}$ on the centerplane as discussed above (Table 2). When the uncertainties were accounted for, the confidence intervals for three of the six cases just mentioned extended across the 1-to-1 line, meaning that as many as 47 of the 50 planes saw improvement with the change to the optimal parameters. In contrast, as many as 22 cases may have not been improved (six plus 16 which have intervals that cross below the 1-to-1 line).

An average of all 50 $corr$ pairs showed an average improvement of $> 16\%$ when $\overline{V_y}$ and $\overline{\omega}$ were considered together. In each of the cases where either GME or $corr$ were not improved by the use of C_{opt}, the results were scarcely worse than when C_{nom} was used. The improvements to GME and $corr$ (and obviously MSE) for the remaining cases were typically much more significant than were the declines in accuracy for the cases where they were worsened.

Cases involving the flight-vehicle configuration deserve special attention since their setup varies the most from the calibration cases. For all six metrics, these data points sit comfortably within the general scatter of all points in the plots, exhibiting no special deviation from the simpler geometries in the smaller-scale wind tunnel. This indicates the robustness of the C_{opt} model and suggests that the pertinent JIC physics are captured by it regardless of what additional geometric complexities are added to the case.

Overall, five of the metrics show anything from a strong improvement in the aggregate of all data sets to a universal improvement. The outlier is the perimeter. The global flow field is improved, the vortex strength and position are improved, but the vortices become more diffused in the process, leading to perimeter error. This perimeter error is greater and more common for the negative vortex situated near the wall for inclined nozzles. Also, in cases where the five successful metrics do not show a clear improvement, it is likely that one or more vortex is in close proximity to the wall. Nonetheless, depending on the engineering application, difficulties with predicting the vortex perimeters may be of lesser consequence than predictions of the vortex circulation and position.

V. Discussion

Some of the results seen here could be partially conjectured from the later papers by Ray et al. In Ray et al. [26], the authors showed that high-order eddy viscosity models will not perform appreciably better than linear eddy viscosity models for the JIC dynamics, when both were tuned to data. This could perhaps indicate that the linear eddy viscosity model was sufficient to get satisfactory answers, provided that its parameters were appropriately calibrated. In Ray et al. [27], the authors tuned the same parameters to three other JIC interactions ((Mach 0.6, $J = 10.2$), (Mach 0.7, $J = 10.2$), and (Mach 0.8, $J = 16.7$)) and obtained estimates of $\{C_\mu, C_{\epsilon 1}, C_{\epsilon 2}\}$ that were similar to C_{opt}, indicating again that the calibrated C_{opt} would generalize beyond the (Mach 0.8, $J = 10.2$) case where C_{opt} was originally learned. The same paper derived analytical values for $\{C_\mu, C_{\epsilon 1}, C_{\epsilon 2}\}$ from first principles (i.e., without any data fitting or assuming that $\alpha = 0$), leading one to conjecture that perhaps the calibrated values of $\{C_\mu, C_{\epsilon 1}, C_{\epsilon 2}\}$ represented physical processes inherent in JIC interactions rather than being artifacts of the fitting process. Consequently, there was some reason to believe that the tuned C_{opt} would be predictive for other interactions, perhaps including the canted jet.

A weakness of the fitting performed in Ray et al. [25, 27] is the use of strong jets ($J = 10.2$, 16.7) that penetrated well into the crossflow and evolved with little interaction with the boundary layers on the wind-tunnel walls. This would indicate that the values of $\{C_\mu, C_{\epsilon 1}, C_{\epsilon 2}\}$ inferred in Ray et al. [25, 27] do not reflect turbulent processes involving CVP-to-boundary layer interactions, and C_{opt} would not be predictive in flows where the jet stays close to the wind-tunnel wall e.g., weak jets ($J = 2.8$, 5.6) and steeply canted jets ($\alpha = 45°$). To a large extent, this paper bears out these conjectures. The use of C_{opt}, represents a nearly 14% increase in C_μ (which increases eddy viscosity), a 9% increase in $C_{\epsilon 2}$ which reduces turbulent dissipation, and a minimal change in $C_{\epsilon 1}$. Together, these actions increase turbulence everywhere. It is likely that this effective increase in turbulence everywhere in the simulation domain resulted in a poorer prediction of the boundary layer. C_{opt} has been shown to be more predictive than C_{nom} in cases where the jet does not interact with the boundary layer. In the cases where it does (because of the cant or the weakness of the jet), C_{nom} remains better than C_{opt} according to some metrics.

It also seems that the increased turbulence that results from the larger C_μ value in C_{opt} corrects the over-penetration of the jet into the freestream seen when using C_{nom}. Arunajatesan [13] reported that turbulence levels in nominal models were likely too low upstream of where the PIV planes were collected—in the nearfield of the jet—and that this resulted in inaccuracies in the jet trajectory and the CVP location. For some variables and features for some cases the move from C_{nom} to C_{opt} resulted in an overcorrection (lowering the jet centerline), but appears to do so as a trade-off for improving the predictions of the peak magnitudes. Additionally, the overcorrection may only be occurring in some portions of the domain while other portions are corrected by the right amount. This was seen in the data for the $\alpha = 0°$, $J = 10.2$ case. The calibration procedure was performed on data from this case by Ray et al. [25] and indeed improved the metric measurements (for both $\overline{V_y}$ and $\overline{\omega}$) at the $x = 321.8$ mm plane, but did so at the expense of the quality of the results at the $x = 215$ mm plane. Arunajatesan [13] also suggested that while an increase in turbulence may be needed in the jet nearfield, a reduction in turbulence may be needed much further downstream. That appears to be supported here. This may point to larger limitations that exist with the structure of the linear RANS model itself.

One such limitation may be the use of constant scalar values for the model parameters. The potential variability of model parameters as a function of flow variables is not accounted for in most traditional RANS codes [29]. A new model that could pick optimal values for the RANS parameters at every location in space, may be capable of producing even better results. Philosophically, this approach would be similar to the zone-dependent k-ϵ parameters demonstrated in Matai and Durbin [53]. The challenge in our case would be determining how to demarcate various zones and how to ensure logical, continuous values of $\{C_\mu, C_{\epsilon 1}, C_{\epsilon 2}\}$ within each zone. Such definitions could further improve results for the cases studied here, but would not generalize to other flows of interest. The data-driven approach proposed in Miller and Beresh [29] may be a viable route to a generalizable version of this same concept. Therein, the authors demonstrated the ability to determine RANS model coefficients directly from experimental data and suggest that those coefficients could then be cast as functions of local state variables also taken from the same experimental data. The present work establishes a baseline for the behavior of a nominal and an optimized RANS model, against which future modeling approaches will be compared. Nonetheless, even the present simple calibration of RANS parameters produces better estimates of SRQs of interest to vehicle designers.

VI. Conclusions

Taken as a whole, the use of C_{opt} produces superior RANS solutions for a family of JIC cases than does using the nominal parameter values. This was demonstrated across a variety of transonic JIC cases with varied jet-to-freestream dynamic pressure ratios and nozzle inclination angles, with the most rigorous test done using PIV data taken in the

vicinity of a full-scale flight vehicle model. A variety of quality metrics were used to quantify the improvements in the simulations and showed that the use of C_{opt} produced superior predictions of the SRQs across all the test cases. Generally, the use of C_{opt} lowered the location and magnitude of the peaks in both $\overline{V_y}$ and $\overline{\omega}$ within the flow volume. This resulted in more accurate predictions of the spatial alignments of the vortex cores of the CVP and in better estimates of both the peak vorticity and total circulation within each core. While the use of C_{opt} did result in more diffuse vorticity fields that led to vortex cores often being larger than in the PIV, the general shapes of those cores and their locations were still improved.

Perhaps the greatest revelation of this work is the apparent near-universality of C_{opt} for these JIC problems, especially those that differ significantly from the original case used in the parameters' derivation. In fact, many of the cases which were significantly physically different from the calibration case showed larger improvements than were seen in the calibration case itself. Although the case on which the calibration procedure was performed did show considerable improvement in MSE—which is essentially the metric that was used for the calibration—it did not show much improvement in $corr$ or GME. Almost every other case showed more improvement in the correlation and GME. The quintessential example of this is the case of the flow around the full-scale flight vehicle model. In that case, the nozzle was larger than in the calibration case, the nozzle was inclined, which it was not in the calibration case, J was larger, more vortex cores were identifiable, the tunnel was larger, and the relief associated with the cylindrical body shape was clearly different. And yet, the use of C_{opt} still significantly improved the modeling prediction of that flow case, a result demonstrated by the quality metrics.

Although further testing could be done on JIC cases of other flow regimes (different Js, subsonic flows, etc), it seems clear from this work that there is something inherent within C_{opt} that makes it nearly universally better than the standard parameter values for simulating the JIC. For every case studied here, the use of C_{opt} produced superior simulation results by at least some metrics than did C_{nom}.

Acknowledgements

The authors wish to acknowledge Amalia Black and Jonathan Murray, both of SNL, for their contributions to the production of the RANS data. This work was supported by the United States Department of Energy via multiple sub-programs under SNL's Advanced Simulation and Computing (ASC) program.

References

[1] Beresh, S. J., Henfling, J. F., Erven, R. J., and Spillers, R. W., "Turbulent Characteristics of a Transverse Supersonic Jet in a Subsonic Compressible Crossflow," *AIAA Journal*, Vol. 43, No. 11, 2005, pp. 2385–2394. https://doi.org/10.2514/1.14575.

[2] Kawai, S., and Lele, S. K., "Large-Eddy Simulation of Jet Mixing in Supersonic Crossflows," *AIAA Journal*, Vol. 48, No. 9, 2010, pp. 2063–2083. https://doi.org/10.2514/1.J050282.

[3] Bogard, D. G., and Thole, K. A., "Gas Turbine Film Cooling," *J. of Propulsion and Power*, Vol. 22, No. 2, 2006, pp. 249–270. https://doi.org/10.2514/1.18034.

[4] Lee, S.-H., "Characteristics of Dual Transverse Injection in Scramjet Combustor, Part 1: Mixing," *J. of Propulsion and Power*, Vol. 22, No. 5, 2006, pp. 1012–1019. https://doi.org/10.2514/1.14180.

[5] Mahesh, K., "The Interaction of Jets with Crossflow," *Ann. Rev. Fluid Mech.*, Vol. 45, No. 1, 2013, pp. 379–407. https://doi.org/10.1146/annurev-fluid-120710-101115.

[6] Karagozian, A. R., "The Jet in Crossflow," *Phys. of Fluids*, Vol. 26, No. 10, 2014. https://doi.org/10.1063/1.4895900, 101303.

[7] Smith, S. H., and Mungal, M. G., "Mixing, Structure and Scaling of the Jet in Crossflow," *J. Fluid Mech.*, Vol. 357, 1998, pp. 83–122. https://doi.org/10.1017/S0022112097007891.

[8] Cortelezzi, L., and Karagozian, A. R., "On the Formation of the Counter-Rotating Vortex Pair in Transverse Jets," *J. Fluid Mech.*, Vol. 446, 2001, pp. 347–373. https://doi.org/10.1017/S0022112001005894.

[9] Brandeis, J., and Gill, J., "Experimental Investigation of Super- and Hypersonic Jet Interaction on Missile Configurations," *J. Spacecraft Rockets*, Vol. 35, No. 3, 1998, pp. 296–302. https://doi.org/10.2514/2.3354.

[10] Cassel, L. A., "Applying Jet Interaction Technology," *J. Spacecraft Rockets*, Vol. 40, No. 4, 2003, pp. 523–537. https://doi.org/10.2514/2.3992.

[11] Peterson, C. W., Wolfe, W. P., and Payne, J. L., "Experiments and Computations of Roll Torque Induced by Vortex-Fin Interaction," *AIAA Paper 2004-1069*, 2004. https://doi.org/10.2514/6.2004-1069.

[12] Beresh, S. J., Heineck, J. T., Walker, S. M., Schairer, E. T., and Yaste, D. M., "Planar Velocimetry of Jet/Fin Interaction on a Full-Scale Flight Vehicle Configuration," *AIAA Journal*, Vol. 45, No. 8, 2007, pp. 1827–1840. https://doi.org/10.2514/1.26485.

[13] Arunajatesan, S., "Evaluation of Two-Equation RANS Models for Simulation of Jet-in-Crossflow Problems," *AIAA Paper 2012-1199*, 2012. https://doi.org/10.2514/6.2012-1199.

[14] Graham, M. J., Weinacht, P., and Brandeis, J., "Numerical Investigation of Supersonic Jet Interaction for Finned Bodies," *J. Spacecraft Rockets*, Vol. 39, No. 3, 2002, pp. 376–383. https://doi.org/10.2514/2.3836.

[15] DeSpirito, J., "Turbulence Model Effects on Cold-Gas Lateral Jet Interaction in a Supersonic Crossflow," *J. Spacecraft Rockets*, Vol. 52, No. 3, 2015, pp. 836–852. https://doi.org/10.2514/1.A32974.

[16] Duraisamy, K., Iaccarino, G., and Xiao, H., "Turbulence Modeling in the Age of Data," *Annual Review of Fluid Mechanics*, Vol. 51, No. 1, 2019, pp. 357–377. https://doi.org/10.1146/annurev-fluid-010518-040547.

[17] Xiao, H., and Cinnella, P., "Quantification of Model Uncertainty in RANS Simulations: A Review," *Progress in Aerospace Sciences*, Vol. 108, 2019, pp. 1–31. https://doi.org/10.1016/j.paerosci.2018.10.001.

[18] Zhang, X., Wu, J., Coutier-Delgosha, O., and Xiao, H., "Recent Progress in Augmenting Turbulence Models with Physics-Informed Machine Learning," *Journal of Hydrodynamics*, Vol. 31, 2019, p. 1153–1158. https://doi.org/10.1007/s42241-019-0089-y.

[19] Cheung, S. H., Oliver, T. A., Prudencio, E. E., Prudhomme, S., and Moser, R. D., "Bayesian Uncertainty Analysis with Applications to Turbulence Modeling," *Reliability Engineering and System Safety*, Vol. 96, No. 9, 2011, pp. 1137–1149. https://doi.org/10.1016/j.ress.2010.09.013.

[20] Edeling, W. N., Cinnella, P., Dwight, R. P., and Bijl, H., "Bayesian Estimates of Parameter Variability in the $k-\epsilon$ Turbulence Model," *Journal of Computational Physics*, Vol. 258, 2014, pp. 73–94. https://doi.org/10.1016/j.jcp.2013.10.027.

[21] Guillas, S., Glover, N., and Malki-Epshtein, L., "Bayesian Calibration of the Constants of the $k-\epsilon$ Turbulence Model for a CFD Model of Street Canyon Flow," *Computer Methods in Applied Mechanics and Engineering*, Vol. 279, 2014, pp. 536–553. https://doi.org/10.1016/j.cma.2014.06.008.

[22] Zhang, J., and Fu, S., "An Efficient Bayesian Uncertainty Quantification Approach with Application to $k-\omega-\gamma$ Transition Modeling," *Computers and Fluids*, Vol. 161, 2018, pp. 211–224. https://doi.org/10.1016/j.compfluid.2017.11.007.

[23] Kato, H., Ishiko, K., and Yoshizawa, A., "Optimization of Parameter Values in the Turbulence Model Aided by Data Assimilation," *AIAA Journal*, Vol. 54, No. 5, 2016, pp. 1512–1523. https://doi.org/10.2514/1.J054109.

[24] Kato, H., Yoshizawa, A., Ueno, G., and Obayashi, S., "A Data Assimilation Methodology for Reconstructing Turbulent Flows Around Aircraft," *Journal of Computational Physics*, Vol. 283, 2015, pp. 559–581. https://doi.org/10.1016/j.jcp.2014.12.013.

[25] Ray, J., Lefantzi, S., Arunajatesan, S., and Dechant, L., "Bayesian Parameter Estimation of a $k-\epsilon$ Model for Accurate Jet-in-Crossflow Simulations," *AIAA Journal*, Vol. 54, No. 8, 2016, pp. 2432–2448. https://doi.org/10.2514/1.J054758.

[26] Ray, J., Lefantzi, S., Arunajatesan, S., and Dechant, L., "Learning an Eddy Viscosity Model Using Shrinkage and Bayesian Calibration: A Jet-in-Crossflow Case Study," *ASCE-ASME Journal of Risk and Uncertainty in Engineering Systems, Part B: Mechanical Engineering*, Vol. 4, No. 1, 2018. https://doi.org/10.1115/1.4037557, 011001.

[27] Ray, J., Dechant, L., Lefantzi, S., Ling, J., and Arunajatesan, S., "Robust Bayesian Calibration of a $k-\epsilon$ Model for Compressible Jet-in-Crossflow Simulations," *AIAA Journal*, Vol. 56, No. 12, 2018, pp. 4893–4909. https://doi.org/10.2514/1.J057204.

[28] DeChant, L., Ray, J., Lefantzi, S., Ling, J., and Arunajatesan, S., "$K-\epsilon$ Turbulence Model Parameter Estimates Using an Approximate Self-similar Jet-in-Crossflow Solution," *AIAA Paper 2017-4167*, 2017. https://doi.org/10.2514/6.2017-4167.

[29] Miller, N. E., and Beresh, S. J., "Using Particle Image Velocimetry to Determine Turbulence Model Parameters," *AIAA Journal*, Vol. 59, No. 3, 2021, pp. 842–854. https://doi.org/10.2514/1.J059741.

[30] Oberkampf, W. L., and Roy, C. J., *Verification and Validation in Scientific Computing*, Cambridge University Press, Cambridge, UK, 2010. https://doi.org/10.1017/CBO9780511760396.

[31] Miller, N. E., Beresh, S. J., and Ray, J., "Validation of Calibrated $k-\epsilon$ Model Parameters for Jet-in-Crossflow," *AIAA Paper 2019-3706*, 2019. https://doi.org/10.2514/6.2019-3706.

[32] Beresh, S. J., Henfling, J. F., Erven, R. J., and Spillers, R. W., "Penetration of a Transverse Supersonic Jet into a Subsonic Compressible Crossflow," *AIAA Journal*, Vol. 43, No. 2, 2005, pp. 379–389. https://doi.org/10.2514/1.9919.

[33] Beresh, S. J., Henfling, J. F., Erven, R. J., and Spillers, R. W., "Crossplane Velocimetry of a Transverse Supersonic Jet in a Transonic Crossflow," *AIAA Journal*, Vol. 44, No. 12, 2006, pp. 3051–3061. https://doi.org/10.2514/1.22311.

[34] Ray, J., Lefantzi, S., Arunajatesan, S., and Dechant, L., "Bayesian calibration of a $k-\epsilon$ turbulence model for predictive jet-in-crossflow simulations," *AIAA Paper 2014-2085*, 2014. https://doi.org/10.2514/6.2014-2085.

[35] Beresh, S. J., Henfling, J. F., Spillers, R. W., and Pruett, B., "Influence of the Fluctuating Velocity Field on the Surface Pressures in a Jet/Fin Interaction," *J. Spacecraft Rockets*, Vol. 55, No. 5, 2018, pp. 1098–1110. https://doi.org/10.2514/1.A34214.

[36] Beresh, S. J., Henfling, J. F., Erven, R. J., and Spillers, R. W., "Vortex Structure Produced by a Laterally Inclined Supersonic Jet in Transonic Crossflow," *J. of Prop. and Power*, Vol. 23, No. 2, 2007, pp. 353–363. https://doi.org/10.2514/1.25444.

[37] Beresh, S. J., Wagner, J. L., Henfling, J. F., Spillers, R. W., and Pruett, B. O. M., "Turbulent Eddies in a Compressible Jet in Crossflow Measured using Pulse-Burst Particle Image Velocimetry," *Phys. of Fluids*, Vol. 28, No. 2, 2016. https://doi.org/10.1063/1.4940677, 025102.

[38] Roy, C., and Oberkampf, W., "A Complete Framework for Verification, Validation, and Uncertainty Quantification in Scientific Computing (Invited)," *AIAA Paper 2010-124*, 2010. https://doi.org/10.2514/6.2010-124.

[39] Oberkampf, W. L., and Smith, B. L., "Assessment Criteria for Computational Fluid Dynamics Validation Benchmark Experiments," *AIAA Paper 2014-0205*, 2014. https://doi.org/10.2514/6.2014-0205.

[40] Beresh, S. J., Miller, N. E., and Smith, B. L., "Practical Challenges in the Calculation of Turbulent Viscosity from PIV Data," *AIAA Paper 2018-2987*, 2018. https://doi.org/10.2514/6.2018-2987.

[41] Sciacchitano, A., and Wieneke, B., "PIV Uncertainty Propagation," *Meas. Sci. Technol.*, Vol. 27, No. 8, 2016, p. 084006. https://doi.org/10.1088/0957-0233/27/8/084006.

[42] Sciacchitano, A., "Uncertainty Quantification in Particle Image Velocimetry," *Meas. Sci. Technol.*, Vol. 30, No. 9, 2019, p. 092001. https://doi.org/10.1088/1361-6501/ab1db8.

[43] So, R. M. C., Sarkar, A., Gerodimos, G., and Zhang, J., "A Dissipation Rate Equation for Low-Reynolds-Number and Near-Wall Turbulence," *Theoret. Comput. Fluid Dynamics*, Vol. 9, 1997, pp. 47–63. https://doi.org/10.1007/s001620050031.

[44] Brinkman, K. W., Calhoon Jr., W. H., and Dash, S. M., "Scalar Fluctuation Modeling for High-Speed Aeropropulsive Flows," *AIAA Journal*, Vol. 45, No. 5, 2007, pp. 1036–1046. https://doi.org/10.2514/1.21075.

[45] Sierra Thermal Fluid Development Team, "SIERRA/Aero Theory Manual – Version 5.4," Sandia National Laboratories, Albuquerque, NM, USA, 2022. https://doi.org/10.2172/1855032.

[46] Arunajatesan, S., and McWherter-Payne, M. A., "Unsteady Modeling of Jet-in-Crossflow Problems," *AIAA Paper 2013-3099*, 2013. https://doi.org/10.2514/6.2013-3099.

[47] Chang, J. C., and Hanna, S. R., "Air Quality Model Performance Evaluation," *Meteorol Atmos Phys*, Vol. 87, 2004, pp. 167–196. https://doi.org/10.1007/s00703-003-0070-7.

[48] Hanna, S., and Baja, E., "A Simple Urban Dispersion Model Tested With Tracer Data From Oklahoma City and Manhattan," *Atmos. Environ.*, Vol. 43, No. 4, 2009, pp. 778–786. https://doi.org/10.1016/j.atmosenv.2008.11.005.

[49] Franzese, P., and Huq, P., "Urban Dispersion Modelling and Experiments in the Daytime and Nighttime Atmosphere," *Boundary-Layer Meteorol.*, Vol. 139, 2011, pp. 395–409. https://doi.org/10.1007/s10546-011-9593-5.

[50] Brown, A. L., Clemenson, M. D., Benson, M., Elkins, C., and Jones, S. T., "An Urban Dispersion Inspired Scenario for CFD Model Validation," *Fire Saf. J.*, Vol. 120, 2021, p. 103130. https://doi.org/10.1016/j.firesaf.2020.103130.

[51] Besnard, A. C., Shoji, T., Schein, S., Harris, E. W., and Karagozian, A. R., "Exploration of Asymmetric Forcing on Mixing and Structural Characteristics for Transverse Jets," *AIAA Paper 2019-0321*, 2019. https://doi.org/10.2514/6.2019-0321.

[52] Shan, J. W., and Dimotakis, P. E., "Reynolds-Number Effects and Anisotropy in Transverse-Jet Mixing," *J. Fluid Mech.*, Vol. 566, 2006, pp. 47–96. https://doi.org/10.1017/S0022112006001224.

[53] Matai, R., and Durbin, P. A., "Zonal Eddy Viscosity Models Based on Machine Learning," *Flow Turbul. Combust.*, Vol. 103, No. 1, 2019, pp. 93–109. https://doi.org/10.1007/s10494-019-00011-5.